Time-Resolved Diagnostics in a Pulsed, Electron Beam-Generated Plasma

Scott G. Walton, Darrin Leonhardt, and Richard F. Fernsler

***Abstract*—Time-resolved ion flux and energy distributions were measured at an electrode located adjacent to a pulsed, electron beam-generated plasma produced in argon. A Langmuir probe was also used to determine time-dependent electron temperature and plasma density. Temporal variations in the incident Ar^+ and Ar^{+2} ion energy and flux were correlated to changes in the electron temperature and plasma density. The evolution of the plasma density and ion flux is understood by considering the loss mechanisms of each ion species.**

***Index Terms*—Ion energy measurement, mass spectrometry, plasma diagnostics, pulsed plasmas.**

I. Introduction

THE U.S. Naval Research Laboratory, Washington, DC, has developed a materials processing system based on an electron beam-produced plasma [1], [2] and found it to be useful in a number of applications, including nitriding [3], etching [4], [5], deposition [6], and polymer modification [6]. The system currently uses a modulated, magnetically confined multi-keV electron beam to produce the plasma. There are several features that distinguish electron beam-generated plasmas from conventional sources (inductively coupled plasmas (ICPs), electron cyclotron resonance (ECRs) discharges, radio frequency (RF), and direct current (dc) discharges, etc.) used in materials processing. These differences are due mainly to the method of plasma generation: ionization by a high-energy electron beam. For example, when the electron beam is collimated by a magnetic field, the ionization or source volume is uniform, well defined, and localized. Since the electron beam cross section relies on the length and width of electron beam source while the range of the beam depends on operating pressure and beam energy, scaling is straightforward and can be accomplished without a loss in ionization uniformity. Moreover, species production by high-energy (>2 keV) electron beams is largely determined by the gas constituents [7], since the ionization cross sections are similar for most gases at high electron energy.

Perhaps the most remarkable feature of these plasmas is the low average electron temperatures ($T_e \approx 0.3$–1.5 eV) [8], which arise from the fact that electron beam-driven ionization precludes the need for externally applied electric fields. In other sources, external fields are used to heat the plasma electrons so that a sufficient number of electrons are energetic enough to ionize the gas and sustain the plasma. In the absence of these fields, the plasma electrons are cooled through inelastic collisions with the background gas or via losses in the plasma fields. A low electron temperature leads to a low plasma potential, so ions incident on grounded walls and substrates exhibit comparatively low energies (<6 eV) [7], [9].

As noted, the electron beam is pulsed, which allows additional capabilities that may be used to further enhance process control and quality. The "steady state" in modulated plasmas, if achieved at all, represents only a fraction of the processing time. Over the course of one period, the plasma undergoes distinct phases that lead to unique and potentially useful changes in the flux of species at processing surfaces. Given these changes, it is useful to characterize the bulk plasma properties and the flux incident to adjacent surfaces in order to more fully optimize a given process.

This paper discusses experiments to characterize electron beam-generated plasmas produced in argon with the goal of developing an understanding of the temporal behavior of the system. Langmuir probe measurements were used to determine bulk plasma properties, and the flux of ion species at an adjacent electrode was measured using a dual energy analyzer/mass spectrometer. The diagnostics were designed to correlate the bulk properties with the ion flux at the electrode as a function of time. The results presented illustrate the unique features of the system and help provide a rudimentary understanding of the underlying physics leading to the observed behavior in argon.

II. Experimental Apparatus

A. Chamber and Plasma Production

The experimental apparatus has been discussed previously [7] and is shown in the schematic of Fig. 1. The system vacuum was maintained by a 2000 l/s turbomolecular pump. High-purity argon (99.999%) was introduced by a mass flow controller (50 sccm) and the operating pressure of 50 mtorr was achieved by throttling the turbo pump. A beam of energetic electrons was produced by a linear hollow cathode [4] pulsed to 2 kilovolts for 6 ms at a 10% duty factor (see Fig. 2). The emergent beam passed through a slot in a grounded anode and was then terminated at a second grounded anode located further downstream. The electron beam volume between the two anodes defines the ionization source volume, with the dimensions set by the slot size (1 cm × 25 cm) and the anode-to-anode length (43 cm). Beam spreading from collisions with the neutral background was strongly limited by a longitudinal magnetic field of 150 Gauss that was produced by a set of external magnetic field coils

Manuscript received August 31, 2004; revised December 9, 2004. This work was supported by the Office of Naval Research.

The authors are with the U.S. Naval Research Laboratory, Plasma Physics Division, Washington, DC 20375 USA (e-mail: sgwalton@ccs.nrl.navy.mil).

Digital Object Identifier 10.1109/TPS.2005.845239

0093-3813/$20.00 © 2005 IEEE

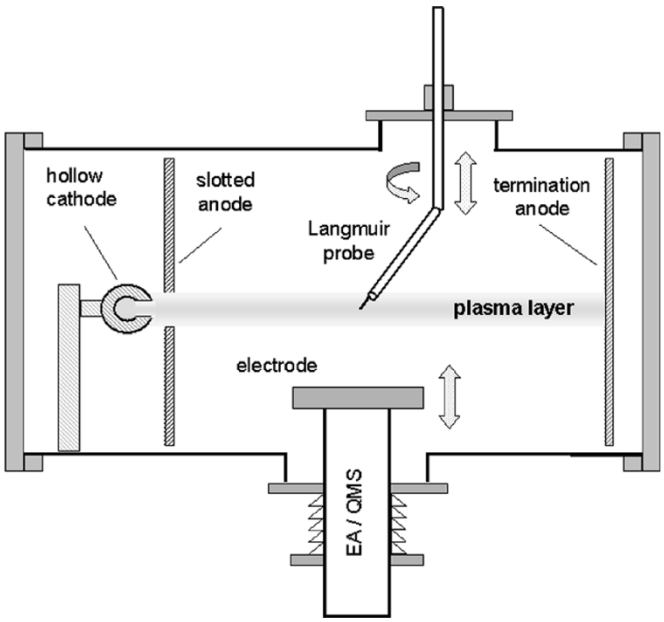

Fig. 1. Schematic of the experimental apparatus. Not shown in the figure are magnetic field coils that produce a longitudinal field.

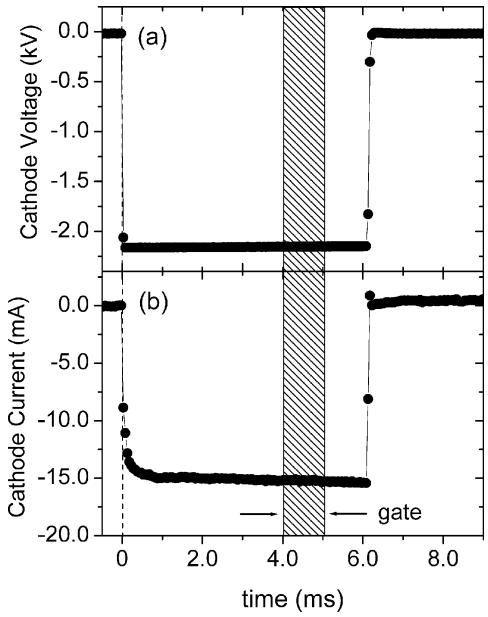

Fig. 2. (a) Cathode bias and (b) current which determined the resulting electron beam energy and current in 50 mtorr argon. The waveform also sets the time scale for data acquisition where the pulse front ($t = 0$) serves as the system trigger and the "gate" indicates the time over which data was accumulated. The gate width is adjustable and the gate could be fixed in time or scanned with respect to $t = 0$.

(not shown). From [1], [2], the employed field keeps the expansion of a 2-keV electron beam in 50 mtorr to <0.5 cm at the termination anode.

B. Plasma Diagnostics

Ion energy distributions and fluxes were measured at the center of a grounded 5.7-cm-diameter stainless steel electrode using a Hiden EQP 300 Plasma Probe. Ions enter the EQP through a 20-μm diameter aperture located in the center of the electrode and are first energy selected by an electrostatic

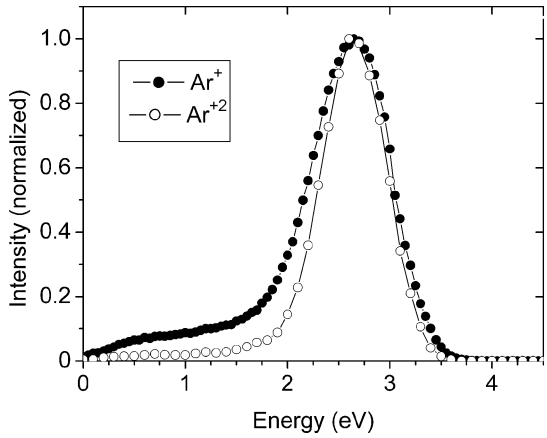

Fig. 3. Normalized ion energy distributions incident to the electrode located adjacent to a pulsed, electron beam generated-plasma produced in 50 mtorr argon. Pulse width was 6 ms (10% duty factor) and the distributions were accumulated during a window extending between 5 and 6 ms.

energy analyzer (EA) and then mass filtered by a quadrupole mass spectrometer (QMS). The energy analyzer has a fixed resolution ($\Delta E/E_t$), and the transmission energy (E_t) was adjusted to provide an uncertainty in energy of approximately $\pm$0.15 eV. The EQP has not been calibrated to determine the absolute flux of each species, so the intensity of the measured signal is reported in arbitrary units; see Fig. 3.

Time-resolved data acquisition using the EQP was accomplished using two gating techniques [10]. First, time-resolved ion energy distributions were measured by gating the EQP such that ion energy distributions were accumulated only during a specified time window (see for example Fig. 2). Alternatively, the real-time output of the EQP was monitored by a dual channel, pulse counter operated in a scanning gate mode, and was used for the time-resolved flux measurements. For either approach, the signal was accumulated over several hundred pulses to keep the average deviation under 10%.

The plasma electron temperature T_e and plasma density n_p, were determined using a Langmuir probe that was mounted on a multi-motion feedthrough and constantly heated with an internal resistive element to reduce surface contaminants. Time-resolved probe techniques [11] entailed stepping the probe voltage in discrete intervals and recording the current as a function of time at each voltage. The characteristic I-V trace was then generated at each time, and the values of T_e and n_p were derived from a best fit of the I-V trace to a Maxwellian electron energy distribution.

III. Results

Typical values for the bias applied to the cathode and the resulting cathode current in 50 mtorr argon are shown in Fig. 2. The extracted electron beam energy was commensurate to the applied bias while current was assumed to be proportional to, but a fraction of the cathode current. Diagnostics to determine electron beam energy and current densities directly are currently under development.

Shown in Figs. 3 and 4 are the Ar^+ and Ar^{+2} ion energy distributions measured at an electrode, located 2.5 cm from the beam axis. The distributions of Fig. 3 were accumulated during

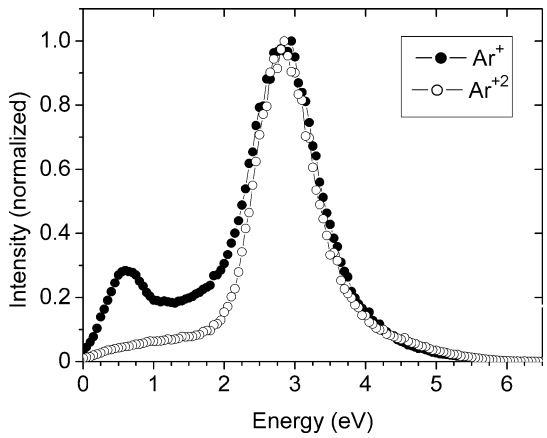

Fig. 4. Normalized ion energy distributions measured during a time window extending between zero and 55 ms.

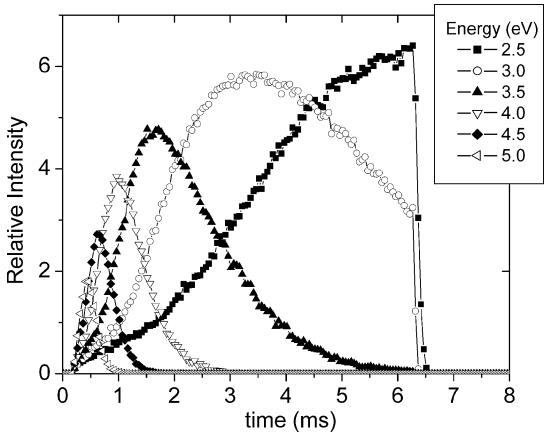

Fig. 5. Time-resolved flux measurements of Ar^{+} ions for energies between 2.5 and 5.0 eV. Energies in this range are only observed during the electron beam pulse.

a 1-ms gate beginning at 5 ms (just prior to the end of the electron beam pulse) and thus best represent the steady state energy distributions. The distributions of Fig. 3 were acquired during a gate extending from zero to 55 ms and include both the beam/plasma initiation and the plasma afterglow. The energy scale of the Ar^{+2} ions has been halved for both figures, to avoid confusion; both ion species must experience the same potential drop across the sheath. It is worth noting that the flux of Ar^{+2} ions is less than 10% of the Ar^{+} ion flux, which was determined by comparing the areas under each raw (nonnormalized) distribution.

Time-resolved Ar^{+} ion flux measurements at fixed energies are shown in Figs. 5 and 6. For these measurements, the energy analyzer was set to pass Ar^{+} ions of a discrete energy, and the signal was accumulated during a 30-μs gate that was scanned in steps of 50 μs up to 9 ms. For times greater than 9 ms, the 30-μs gate was stepped in 200 μs increments. Although not shown, the Ar^{+2} ion flux measurements yielded similar results. That is, the peak intensity of Ar^{+} and Ar^{+2} ions with the same energy occur at the same time. The slight offset in the data is due to the time-of-flight in the EQP.

The *total* Ar^{+} and Ar^{+2} ion fluxes were approximated by the sum of the energy-resolved fluxes, and those results are shown

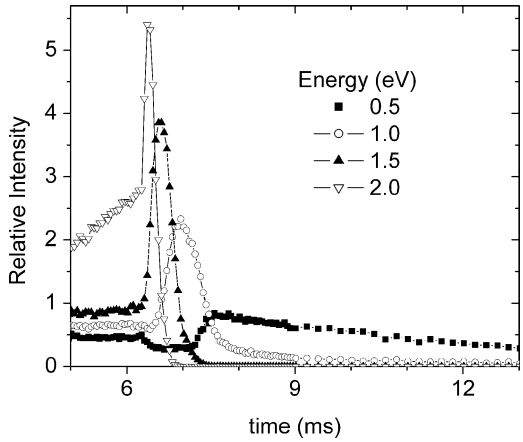

Fig. 6. Time-resolved flux measurements of Ar^{+} ions for energies between 0.5 and 2.0 eV. Lower energy ions are present during all phases of plasma production but dominate the afterglow.

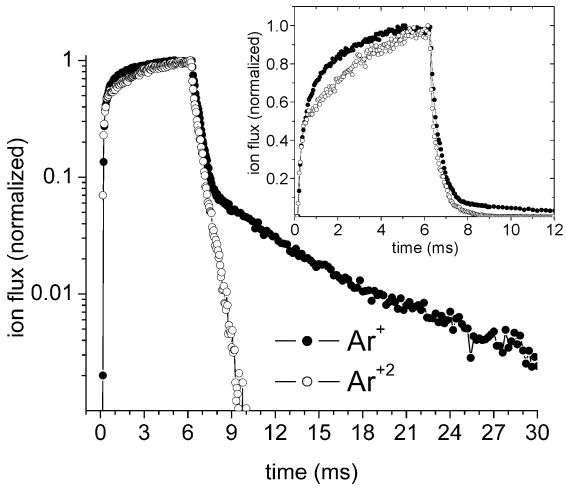

Fig. 7. Normalized total Ar^{+} and Ar^{+2} flux accumulated over all times. Inset: detail of total ion flux during the electron beam pulse. Total flux is determined by summing the fluxes measured in Figs. 5 and 6.

in Fig. 7 on both logarithmic and linear (inset) scales. To ensure a correct representation of the total ion flux, the energy-resolved fluxes must span the entire range of incident energies (see the energy distributions from Fig. 4) and be partitioned equally, with proper attention given to the passband of the energy analyzer. In the case of the Ar^{+} ions, 14 separate energy-resolved fluxes spanning the range from 0 to 6.5 eV were taken in 0.5 eV increments. Given the energy uncertainty ($\pm$0.15 eV), the flux shown in Fig. 7 is a reasonable representation of the total ion flux. The total Ar^{+2} ion flux was found in the same fashion.

Shown in Fig. 8 are time-resolved values of T_e and n_p determined from the Langmuir probe measurements. The probe was located on the beam axis and directly above the center of the electrode, which was located 2.5 cm away.

IV. Discussion

Temporal behavior aside, electron beam-generated plasmas are characterized by low ion energies (Figs. 3 and 4) and large plasma densities (Fig. 8), features that are useful in a number of plasma processing applications. Of interest here, however, is the

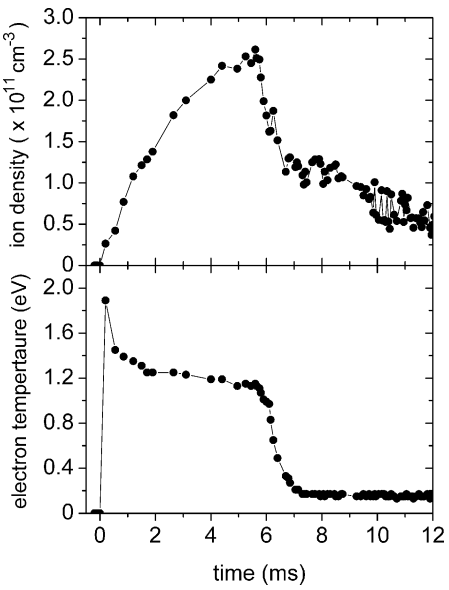

Fig. 8. Time-resolved electron temperature and plasma density measured on the electron beam axis.

time-dependent behavior of the ion energy and flux. To assess that behavior, we assume the plasma potential is in equilibrium with the electron temperature. Consider first the ion energy and the relationship to the electron temperature. For a collisionless sheath, the incident ion energy E_i is determined by the ion kinetic energy at the presheath-sheath boundary E_{ps} and by the potential drop V_s across the sheath [12]:

$$E_i = E_{ps} + eV_s = kT_e\left[\frac{1}{2} + \ln\sqrt{\frac{M_i}{2\pi m_e}}\right] \tag{1}$$

where k is Boltzmann's constant, M_i is the ion mass, and m_e is the electron mass. Given the variation in T_e over the entire period (Fig. 8), a large spread in ion energy is expected in Fig. 4. Conversely, the narrow distributions seen in Fig. 3 are consistent with the near steady values of T_e over that time span.

The time-resolved Ar^+ ion flux measurements of Figs. 5 and 6 give a more detailed description of the incident ion energy. These results show a higher energy immediately after the beam is initiated, a reduction in energy toward the end of the pulse, and an afterglow dominated by low-energy ions. As expected from (1), this behavior follows directly from the evolution of T_e plotted in Fig. 8. It should be noted that separate Langmuir probe measurements show a decrease in both T_e and n_p with distance from the electron beam. Thus, the measured ion energies will not agree exactly with T_e from (1) since the probe data of Fig. 8 is measured on the electron beam axis. Regardless, the temporal behaviors of the ion energies and T_e are in good qualitative agreement.

Consider now the ion flux, Γ_i, leaving the plasma, which can be related to the plasma density [13]

$$\Gamma_i \approx n_s u_b = \alpha n_o\sqrt{\frac{kT_e}{M_i}} \tag{2}$$

where $u_b = (kT_e/M_i)^{1/2}$ is the Bohm velocity, n_s is the ion density at the presheath-sheath boundary, n_o is the on-axis plasma density measured by the Langmuir probe, and α is a constant. The density measurements of Fig. 8 agree qualitatively with the total flux measurements of Fig. 7, as predicted in (2). However, the time scales differ for the Ar^+ and Ar^{+2} ion fluxes; the difference is slight during the electron beam pulse but more striking in the afterglow, where the Ar^+ signal decays much slower. These differences may be understood in terms of the loss mechanisms for each species, namely charge exchange and neutralization at the walls.

To understand the density evolution, assume the ion density $n_i(t)$ for a given species (i) varies in time as

$$\frac{dn_i}{dt} = S_i - k_r n_e n_i - k_c n_g n_i - \frac{D_a}{l^2}n_i. \tag{3}$$

Here, S_i is the ionization rate, k_r is the electron-ion recombination coefficient, k_c is the ion destruction coefficient due to charge exchange, D_a is the ambipolar diffusion constant, l is the source-electrode distance, n_g is the neutral density, and n_e is the electron density. The electron-ion recombination rate coefficient is small $(k_r \sim 10^{-13}\ \mathrm{cm^3 \cdot s^{-1}})$ for atomic ions [14], and for the densities in these plasmas, the second term on the RHS of (3) can be neglected. Thus

$$\frac{dn_i}{dt} = S_i - \beta n_i \tag{4}$$

where $\beta = [k_c n_g + (D_a/l^2)]$. When the beam is on, i.e. $S_i > 0$, (4) can be integrated to obtain

$$n_i = n_{si}\left(1 - \exp(-\beta t)\right) \tag{5}$$

where $n_{si} = S_i/\beta$ is the steady-state ion density. If the beam is turned off at t_o (i.e., $S_i = 0$ for $t > t_o$), the solution in the afterglow becomes

$$n_i = n_{si}\exp\left(-\beta(t - t_o)\right). \tag{6}$$

The time-dependent behavior of the ion densities and thus fluxes depend strongly on ion- and electron-neutral interactions, specifically charge exchange reactions and ambipolar diffusion. The charge exchange term is meaningful only for $Ar^{+2} + Ar \rightarrow 2Ar^+$ since resonant charge exchange involving Ar^+ ions has no effect on the Ar^+ ion density.

Since diffusion is comparable for the two ions, charge exchange alone largely determines the differences in species evolution.

The presence of the magnetic field influences ion diffusion by reducing the electron flow across the magnetic field

$$D_a = \frac{T_e}{M_i\nu_i + m_e\nu_e^*} \tag{7}$$

where $\nu_{i,e}$ is the electron or ion-neutral collision frequency, and

$$\nu_e^* = \nu_e\left(1 + \frac{\Omega_e^2}{\nu_e^2}\right) \approx \frac{\Omega_e^2}{\nu_e} \tag{8}$$

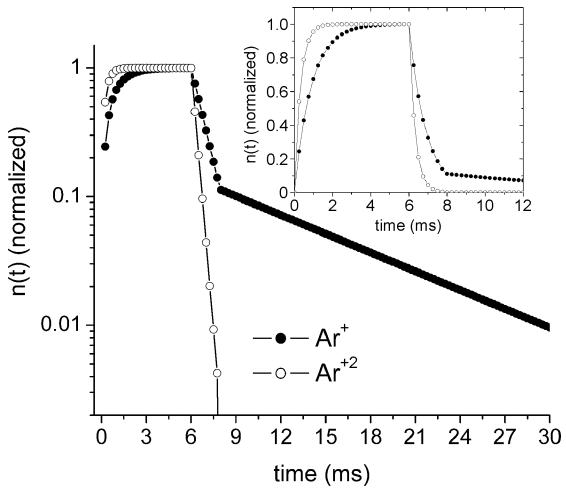

Fig. 9. Time-dependent ion densities calculated from (5) and (6). Values used in the equations where chosen to best approximate the results of Figs. 7 and 8.

since the electron gyrofrequency $\Omega_e \gg \nu_e$ for a 150 Gauss magnetic field. Over the range of electron temperatures measured (0 to 2.0 eV), the electron collision frequency varies appreciably due to the Ramsauer effect [15]. However, for $T_e = 1.0$ eV and $T_e = 0.1$ eV, the electron-neutral collision cross section $\sigma_e \approx 10^{-16}$ cm^2 [15], Thus, for thermal ions with collision cross sections $\sigma_i(\mathrm{Ar}^+) = 2.6 \times 10^{-14}$ cm^2 and $\sigma_i(\mathrm{Ar}^{+2}) = 3.5 \times 10^{-14}$ cm^2 [16], we estimate that for $T_e = 1.0$ eV

$$D_a(Ar^+) \approx D_a(Ar^{+2}) \approx 2 \times 10^3 \,\mathrm{cm}^2 \cdot \mathrm{s}^{-1} \tag{9}$$

and for $T_e = 0.1$ eV

$$D_a(Ar^+) \approx D_a(Ar^{+2}) \approx 100 \,\mathrm{cm}^2 \cdot \mathrm{s}^{-1}. \tag{10}$$

From the T_e data in Fig. 7, the ambipolar diffusion constants of (9) and (10) would roughly correspond to the steady-state and far afterglow phases of plasma production, respectively.

Calculations of the ion densities derived from (5) and (6) are shown in Fig. 9. The quantities chosen for the calculations provide the best agreement with the data and include: for times up to 8 ms, $D_a = 7 \times 10^3$ cm^2·s^{-1}, for times exceeding 8 ms, $D_a = 700$ cm^2·s^{-1}, and a charge exchange rate, $k_c = 10^{-12}$ cm^3·s^{-1}. The values of D_a chosen are higher than the estimates of D_a in (9) and (10) and the temporal behavior of the densities are clearly not in exact agreement with the experimental data. However, the general trends are similar and the results provide useful insight. First, the electron contribution to ambipolar diffusion in (7) is not easily determined but must be considered, since the unmagnetized diffusion coefficient, $D_i = T_e/M_i\nu_i$, is far too large. Second, the long-lasting flux of Ar^+ ions observed at the electrode clearly requires a significant decrease in the diffusion rate, and this decrease is attributed to the large drop in T_e. Lastly, charge exchange dominates the behavior of Ar^{+2} and the rate above is close to the published rates for the reactions of the ^{1}D and ^{1}S metastable states [17]. This choice works well in the afterglow but not while the beam is on; using the rate for the ^{3}P ground state [17] produces better results in that phase. Clearly, a more sophisticated approach is required, particularly in the regions where the plasma parameters change abruptly. Such an approach might include an electron beam propagation model, a fluid model of plasma flow, and a field solver to model the sheath and the resulting incident ion energies.

V. Summary

The diagnostics in this work were aimed at providing a time-dependent description of pulsed, electron beam-generated plasmas produced in argon. A Langmuir probe was used to determine the plasma density and electron temperature, and a dual energy analyzer/mass spectrometer was used to measure the incident Ar^+ and Ar^{+2} ion energies and fluxes at an electrode located adjacent to the plasma. The two diagnostics provide a means to correlate the bulk plasma properties with the ion flux at the surface.

There was good agreement between the temporal variations in the ion energies and electron temperature and similarly good agreement between the flux and the plasma density. Simple models were constructed to explain these results and indicate recombination at the walls was found to be the dominant loss mechanism for Ar^+ ions, while Ar^{+2} ions were destroyed mainly by charge exchange. Magnetization of the plasma electrons was also found to play a significant role in the diffusion of ions. A more detailed model is required to fully understand the behavior of the plasma, but the simple approach used here provides a reasonable first step in describing the gas-phase dynamics in electron beam-generated plasmas.

References

[1] R. F. Fernsler, W. M. Manheimer, R. A. Meger, J. Mathew, D. P. Murphy, R. E. Pechacek, and J. A. Gregor, "Production of large-area plasma by electron beams," *Phys. Plasmas*, vol. 5, pp. 2137–2143, 1998.

[2] W. M. Manheimer, R. F. Fernsler, M. Lampe, and R. A. Meger, "Theoretical overview of the large-area plasma processing system (LAPPS)," *Plasma Sources Sci. Technol.*, vol. 9, pp. 370–386, 2000.

[3] C. Muratore, D. Leonhardt, S. G. Walton, D. D. Blackwell, R. F. Fernsler, and R. A. Meger, "Low temperature nitriding of stainless steel in an electron beam generated plasma," *Surf. Coat Technol.*, vol. 191, pp. 255–262, 2005.

[4] D. Leonhardt, C. Muratore, S. G. Walton, D. D. Blackwell, R. F. Fernsler, and R. A. Meger, "Generation of electron-beam produced plasmas and applications to surface modification," *Surf. Coat Technol.*, vol. 177–178, p. 682, 2004.

[5] D. Leonhardt, S. G. Walton, C. Muratore, R. F. Fernsler, and R. A. Meger, "Etching with electron beam generated plasmas," *J. Vac. Sci. Technol.*, vol. 22, pp. 2276–2283, 2005.

[6] D. Leonhardt, C. Muratore, S. G. Walton, and R. A. Meger, "Plasma enhanced surface treatments using electron beam-generated plasmas," *Surf. Coat Technol.*, vol. 188–189, pp. 299–306, 2004.

[7] S. G. Walton, C. Muratore, D. Leonhardt, R. F. Fernsler, D. D. Blackwell, and R. A. Meger, "Electron beam-generated plasmas for materials processing," *Surf. Coat Technol.*, vol. 186, pp. 40–46, 2004.

[8] D. Leonhardt, S. G. Walton, D. D. Blackwell, W. E. Amatucci, D. P. Murphy, R. F. Fernsler, and R. A. Meger, "Plasma diagnostics in LAPPS," *J. Vac. Sci. Technol. A, Vac. Surf. Films*, vol. 19, pp. 1367–1373, 2001.

[9] S. G. Walton, D. Leonhardt, D. D. Blackwell, R. F. Fernsler, D. P. Murphy, and R. A. Meger, "Ion energy distributions in a pulsed, electron beam-generated plasma," *J. Vac. Sci. Technol. A, A, Vac. Surf. Films*, vol. 19, no. 4, pp. 1325–1329, 2001.

[10] ——, "Time-resolved ion flux measurements in pulsed, electron beam-generated plasmas," *Phys. Rev E, Stat. Phys. Plasmas Fluids Relat. Interdiscip. Top.*, vol. 65, 2002.

[11] D. Leonhardt, W. Amatucci, and G. Gatling, "Temporally Resolved Langmuir Probe Measurements in LAPPS,", U.S. Naval Res. Lab. Memo. Rep. NRL/MR/6750-04-8761, 2004.
[12] M. A. Lieberman and A. J. Lichtenberg, *Principles of Plasma Discharges and Materials Processing*. New York: Wiley, 1994, ch. 6.
[13] M. A. Liebermann and S. Ashida, "Global models of pulse-power-modulated high-density, low-pressure discharges," *Plasma Sources Sci. Technol.*, vol. 5, pp. 145–158, 1996.
[14] D. R. Bates and A. Delgarno, *Atomic and Molecular Processes*. New York: Academic, 1962.
[15] L. S. Frost and A. V. Phelps, "Momentum-transfer cross section for slow electrons in He, Ar, Kr, and Xe from transport coefficients," *Phys. Rev.*, vol. 136, pp. A1538–A1545, 1964.
[16] A. V. Phelps, "The application of scattering cross sections to ion flux models in discharge sheaths," *J. Appl. Phys.*, vol. 76, pp. 747–753, 1994.
[17] R. Johnson and M. A. Biondi, "Measurements of radiative charge-transfer reactions of doubly and singly charged rare gas ions with rare-gas atoms at thermal energies," *Phys. Rev A, Gen. Phys.*, vol. 18, pp. 996–1003, 1978.

Scott G. Walton was born in Lancaster, PA, on December 23, 1968. He was received the B.S. degree in physics from Bloomsburg University of Pennsylvania, Bloomsburg, in 1991 and the M.S. and Ph.D. degrees in physics from the College of William and Mary, Williamsburg, VA, in 1994 and 1998, respectively.

He joined the U.S. Naval Research Laboratory, Plasma Physics Division, Washington, DC, in 1998 as a National Research Council Postdoctoral Research Associate and as a Scientist with SFA, Inc., Largo, MD, before becoming a Staff Member in 2002. His research is focused on plasma generation, plasma characterization, and plasma processing, including an interest in new approaches to plasma-based materials modification.

Dr. Walton is Member of the American Vacuum Society and the Society of Vacuum Coaters.

Darrin Leonhardt was born in Brook Park, OH. He received the B.S. degrees in physics and chemistry from Kent State University, Kent, OH, in 1988 and the Ph.D. degree in chemical physics from the University of Maryland, College Park, in 1995.

From 1995 to 1998, he was a National Research Council Postdoctoral Research Fellow in the Chemistry Division at the U.S. Naval Research Laboratory (NRL), Washington, DC. Since 1998, he has been a Research Physicist in the Plasma Physics Division at NRL. Current research interests include plasma modification of materials and surfaces, as well as the fundamental properties of these plasmas.

Dr. Leonhardt is a Member of the American Physical Society and is presently on the Executive Board of American Vacuum Society's Plasma Science and Technology Division.

Richard F. Fernsler received the Ph.D. degree in plasma physics from the University of Maryland, College Park, in 1976.

He worked as a National Research Council Postdoctoral Associate at the U.S. Naval Research Laboratory, Washington, DC, until 1977, at which point he joined JAYCOR, Inc. Since 1983, he has been at the U.S. Naval Research Laboratory, Washington, DC. His research has included theoretical investigations of electrical streamers, lightning, glow discharges, laser and microwave breakdown, electron beam propagation, and plasma processing.